Microcapillary film reactor outperforms single-bore mesocapillary reactors in continuous flow chemical reactions

Kirandeep K. Gill[1], Rachel Gibson[1], Kam Ho Chester Yiu[1], Patrick Hester[2] and Nuno M. Reis[1]

[1]*Department of Chemical Engineering and Centre for Biosensors, Bioelectronics and Biodevices (C3Bio), University of Bath, Claverton Down, Bath BA2 7AY, UK*

[2]*Lamina Dielectrics Ltd, Billingshurst RH14 9TF, UK*

Meso- and micro-flow reactors are routinely used in continuous flow chemistry, however the role of capillary diameter, *D*, on conversion and reaction rates is often overlooked during scaled-up. Volume, pressured drop and diffusion distances/times must be delicately balanced to fully realize the hydrodynamic capabilities of continuous chemical flow reactors. We carried out a comprehensive Computational Fluid Dynamics analysis experimentally validated with detailed fluid tracing, residence time distributions and continuous chemical reactions (neutralization and 4th Bourne reaction) to fully elucidate the role of *D* and molecular diffusion in reagents dispersion and chemical conversion. To our understanding, we captured and reported both numerically and experimentally for the first time the transition from convective, segregated flow to plug flow and dispersed flow, which we propose is linked to a dimensionless ratio between time scales of diffusion to convection, t_{diff}/t_{conv}. We tested three tubular systems: a small-bore (i.d. ~1,100 µm) and large-bore (i.d. ~2,400 µm) capillary reactors and a novel multiplexed (10-bore) Microcapillary Film Reactor (MFR) with mean i.d. 363±32.2 µm. In the MFR's narrow microcapillaries we observed excellent radial diffusion linked to the small diffusion distance, with low dimensionless axial dispersion coefficient values (D_{ax}/uL) ranging from 0.0015±0.0005 to 0.0033±0.0006 (for flow rates 0.5-5.0 mL/min), exhibiting all the desired features of a high-performance 'plug' flow system. D_{ax}/uL remained mostly independent of the Reynolds number, whereas for the single, large bore capillary the D_{ax}/uL values (0.032–0.057) increased linearly with the Reynolds numbers (19.4–48.5), shifting towards very dispersive flow. We propose splitting flow through multiple parallel microcapillaries as in the MFR is a superior strategy for scaling-up continuous flow reactions compared to increasing *D,* which neglects diffusive effects.

Keywords: Tubular microreactors, residence time distribution, flow chemistry, Microcapillary Film Reactor, continuous manufacturing; new dimensionless number

1. Introduction

Batch chemical processing is bounded by important limitations including temperature and concentration gradients and high molecular weight distributions [1]. These performance restrictions outweigh their versatility and flexibility, leading the way to continuous flow chemistry which is rapidly gaining momentum as reactions in tubular reactors offer benefits of inherent safety characteristics, controlled reactions conditions and enhanced heat and mass transfer for higher space-time yields [2]–[5]. This has shifted interest to the development of micro and meso-flow reactors suited for continuous flow with the core belief that reacting reagents in a single small-bore microchannel results in a narrow residence time distribution (RTD) with enhanced radial micromixing, translating into improved reaction rates, selectively, product yields and impurity control [6]. However, selection of the inner diameter, *D,* for the tubular reactor is currently done empirically and as the volume of the sample tends to be a limiting factor, there is extensive flow chemistry literature ignoring the relevance of diffusive effects and using single large-bore (LB) capillaries [7]–[9]. Presently, a clear understanding of the influence of *D* on the hydrodynamic and chemical conversion capabilities of tubular reactors is urged, but also a more linear approach to scaling-up continuous tubular flow reactors.

The field of flow technologies for chemical applications may be classified as microreactors (~10-500 μm) or meso/macro reactors (up to 4.6 mm channel width) for scale-up production [10]. Mesoreactors offer improved flow capacities, lower pressure drops (ΔP) and a low chance of channel blocking [11]. Microreactors offer uniform temperature control, high surface-to-volume ratios and well defined flow patterns [12]. Theoretically the use of small *D* is desirable for delivering ideal plug flow due to the shorter diffusion times, following Einstein's law of diffusion, yet this imposes limitations of small internal volumes (V) and large ΔP which may

be overcome by scaling-up to large bore capillaries. On the other hand, the reaction time becomes shorter than the mixing time in large bore capillaries and leads to lower microreactor performance and increased byproduct formation [13]. To achieve higher efficiencies in LB capillaries, internal structures are often introduced to increase the interfacial contact area and speed up the mixing, however this has been found to significantly affect the ΔP and requires complex microfabrication [14]. Periodic structures are an alternative for scaling up chemical reactions because of easy optimization, however fluid access to individual reactors must be uniform and homogenous [15].

The optimum flow microreactor for a desired reaction may be designed by matching characteristics to the reaction kinetics [16], [17]. Chemical reactions with a high reaction rate constant (k), such as neutralization reactions, are strongly influenced by the rate of mixing and have a small chemical timescale (τ_c) less than 1 s, whereas a small k ($1\ \text{s} < \tau_c < 10$ mins) indicates reactions are mostly kinetically controlled but may still benefit from microstructure devices [18], [19]. However, the parabolic velocity profile, characteristic of laminar flow, within microreactors results in high axial dispersion of fluid elements and limited mass transfer capabilities [20]. Microreactor designs aim to enhance radial mixing which is vital for a high performance microreactor, especially for reaction systems with side reactions or consecutive reactions [21]. Controlled mixing of reagents is important in regulating and monitoring reaction rates, where reaction time is directly proportional to the microchannel length [22]. The impact of the micromixer type has also been found to be significant for yield, with the multilamination type, such as an arrowhead-mixer, being most suitable for mixing-controlled reactions [14], [23]. Adding lateral structures to microchannels promotes micromixing, with mixing efficiency further influenced by the Reynolds number (Re) [24], [25]. In-line static mixers in tubular reactors promote homogenous mixing for improved continuous flow reactions, however they

are prone to clogging with viscous solutions [26]. Although the relation between mixing and reaction rate has been explored, there are very few works in literature focusing on the optimization of microreactors [27].

The RTD is a significant index for understanding the fluid flow profile and enables the exact prediction of yield for first order reactions [28]. The effect of the RTD on reaction progress is a function of chemical kinetics and conversion, where kinetics in tubular microreactors may be defined by the extent of axial dispersion and mean residence time. Curvature of tubular reactors induces radial mixing through Dean forces, though the effect is not always strong enough to fully eliminate the parabolic velocity profile [16], [29]. Temperature differences between the fluid and channel wall have also been applied to perturb the parabolic profile in a flow tube reactor [30]. Droplet based microreactors with narrow RTDs in each slug have also been employed for flow based syntheses [31], [32]. Micromixing behavior has been studied in continuous flow oscillatory baffled reactors using the RTD and has been explored as a process intensification strategy in carboxylic acid esterification's, imine and metal-organic frameworks syntheses [33]–[36]. The breadth of the RTD has strong, statistical correlations with reaction conversion in continuous flow and narrow RTD has been found to increase conversion rates in a range of chemical reactions including Krapcho dealkoxycarbonylation reactions, consecutive reactions and exothermic Michael additions [37]–[40].

Realizing the delicate balance between volume, pressured drop and diffusion time/distance in the selection of D is crucial for optimal hydrodynamic control of tubular flow (micro)reactors. In this study, we present for the first time a comprehensive Computational Fluid Dynamics (CFD) study that unravels the role of D and molecular diffusion coefficients (D_m) on flow transition between highly dispersive laminar (convective) flow and ideal plug flow in tubular

micro- and meso-flow systems. We compared the extent of micromixing achieved in single-small bore and large bore microreactors with a 10-bore Microcapillary Film Reactor (MFR), having internal diameters (i.d.) of 1,100 μm, 2,400 μm and 363±32.2 μm respectively. Hydrodynamic characteristics were experimentally validated using tracer breakthrough curves, neutralization and acid-catalyzed hydrolysis (4th Bourne reaction) continuous flow reactions, all well-documented and reliable methods for quantifying the extent of micromixing and characterizing the performance of continuous chemical flow systems.

2. Materials and methods

2.1. Materials

The neutralization and 4th Bourne reaction used reagent grade (98%) dimethoxypropane (DMP), reagent grade sodium hydroxide pellets (>99%) and sodium chloride (>99.5%) supplied by Sigma Aldrich Ltd (Dorset, UK). Absolute ethanol (>99%), methanol, acetone and hydrochloric acid (5M) were supplied by Fisher scientific (Loughborough, UK). The bromothymol blue indicator for the neutralization reaction was supplied by Fisher scientific (Loughborough, UK). RTD measurements used Indigo Carmine dye supplied by Sigma-Aldrich (Dorset, UK).

2.2. Tubular microreactors

Small single bore capillaries (i.d. 1,100 μm) of length 7.39 m (Figure 2b) and large bore single capillaries (i.d. 2,400 μm) with length 1.7 m (Figure 2c) were fabricated from Teflon® FEP (fluorinated ethylene propylene) tubing and sourced from Adtech Polymer Engineering Ltd (Stroud, UK). These diameters were selected as they are typical of those used in commercial

flow chemistry systems. The small and large single bore reactors were coiled around a helical coil with diameter around 100 mm. A novel microcapillary film (Figure 2a) consisting of a flat plastic film having an array of 10 parallel microcapillaries with mean i.d. 363±32.2 μm was mass-manufactured by Lamina Dielectrics Ltd (Billingshurst, UK) from Teflon® FEP using a continuous melt-extrusion process [41]. The small inner diameter of the MCF material is sufficiently small to still experience the effects of molecular diffusion without the impractical pressure drops and reduced volumes of very narrow microcapillaries. On a previous study by Hornung et al. [42], a 33 meter long 10-bore MCF disc with mean inner diameter 200 μm was used in continuous flow chemistry applications, with a reported pressure drop, ΔP of 13 bar at a flow rate of 1 mL/min By nearly doubling the inner diameter from ~200 μm to 363 μm, based on Hagen-Poiseuille equation, the pressure drop per unit length was reduced by around 11-fold, furthermore decreasing the length from 33 m down to just 7 m reduced the total pressure drop by >50-fold.For the flow rates (0.5 – 5 mL/min) and length used for the MFR, we estimated a pressure drop between 0.09 - 1.1 bar with differences for each flow rate ranging from 5-15%, making the system compatible with low-cost pumping equipment. As pressure drop is highly dependent on inner diameter of the capillaries, we expect a mean variance of 8-9 % can represent up to ~40% difference on the volumetric flow rate split across the microcapillary strip. Yet, this difference is anticipated to be smaller for the superficial flow velocity which is dependent on the capillary cross section (area). The microcapillary film has exceptional optical properties, resulting from a refractive index matching water, for a high signal-to-noise ratio [43], therefore enabling non-invasive optical imaging. The MFR consists of an aluminium etch alloy case (Lamina Dielectrics Ltd., UK) holding 7.39 m of microcapillary film material (Figure 2a). Minimal distortion of the capillary cross-sections was expected in the MFR coiling arrangement due to the large bending diameters (29.4 – 46.1 mm) of the MFR corners and high flexibility of the Teflon® FEP material. Two SPM 100 Syringe

Pumps (SIMTech Microfluidics Foundry, Singapore) were connected to the MFR using a push fit polyetheretherketone (PEEK) T-valve connector (Sigma Aldrich Ltd, UK). The microcapillary film in the MFR was fitted with a specialized connector built in-house (see Figure S1 in supplementary material for a detailed experimental setup). A microcapillary film with 19 capillaries (D=~230 μm) fabricated from linear-low-density polyethylene (LLDPE) has been previously formed into spiral structures by a heat melding process for continuous flow chemical reactions [44]. However, their experimental setup utilized epoxy resin connectors (making the capillaries prone to blockages) / plastic fittings and the 19 capillaries had a large deviation from mean capillary D (15.5%) [45]. Our design offers better heat distribution to all capillaries, compared to the spiral structures, via the alloy casing and higher chemical and heat resistance with the Teflon® FEP material.

2.3. Measurement of RTD

A step input with tracer injection followed by buffer washout was used to measure RTD in the MFR, small bore and large bore reactors, all having the same internal hydraulic volume (7.7 ml). Indigo carmine tracer dye (15000 ppm) was injected into the system inlet using syringe pumps at a constant rate (step input) and concentration was measured at the outlet as a function of time by converting greyscale images from XS USB 2.0 μEye XS camera (IDS Imaging (Obersulm, Germany) into absorbance. Two syringe pumps separately filled with deionized (DI) water and tracing dye were connected into the reactors. The reactors were initially primed with water, after which 15 ml of dyed solution was pumped into the system at flow rates of 0.5, 1.0, 1.5, 2 and 5 ml/min and the outlet concentration measured. Lighting was provided by a UVP-BioLite Transilluminator (Ultra-Violet Products Ltd., UK) fitted with an external green filter (Edmund Optics Ltd, UK) and white LED backlight (IO Rodeo Inc, US). The washout step was generated by switching the inlet feed to DI water.

2.4. Analytical modelling of RTD and axial dispersion

The cumulative age distribution curve F(t) defined in Equation 1 can be calculated from the outlet concentration (c_{out}) and maximum outlet concentration ($c_{out,max}$) at the outlet of the reactor:

$$F(t) = c_{out\,(t)}/c_{out,max} \tag{1}$$

F(t) and the exit age distribution, E(t), represent the RTD and may be transformed between each other over time (t) as shown in Equation 2 and 3 [46]:

$$E(t) = dF(t)/dt \tag{2}$$

$$F(t) = \int_0^t E(t)dt \tag{3}$$

The F(t) and E(t) curves are often normalized for comparison of systems using the normalized flow time, θ, via $\theta = t/\bar{t}$ where $\bar{t}$ is the experimental mean residence time. The axial dispersion model was used to quantify deviations from ideal plug flow using the dispersion number, D_{ax}, which quantifies the extent of axial dispersion with respect to superficial fluid velocity, u, and reactor length, L, and is determined by Equation 4 [47]:

$$E_\theta = \tau E(t) = \frac{1}{\sqrt{4\pi(D_{ax}/uL)}} exp\left[-\frac{(1-\theta)^2}{4(D_{ax}/uL)}\right] \tag{4}$$

The axial dispersion model considered reactors as having open-open boundary conditions as dispersion occurs both upstream and downstream of the reaction which fairly recreated the experimental RTD and CFD boundary conditions as no secondary mixing is expected through the boundaries. The axial dispersion model in a capillary with radius, r (for circular capillary

r=D/2), and maximum velocity, u_{max}, may be expanded to introduce molecular diffusion effects using an effective diffusion coefficient, D_{eff} [48], defined in Equation 5:

$$D_{eff} = D_m + \frac{r^2 u_{max}^2}{192 \cdot D_m} \quad (5)$$

2.5. CFD modelling

ANSYS Fluent Inc. 19.3 was used to numerically simulate 2D fluid flow in straight microchannels having internal diameters of 400, 1,100 and 2,400 µm, and domain length 240 mm using the finite volume method and an axisymmetric setup [49]. We used the pressure-based solver and SIMPLE (Semi-Implicit Method for Pressure-Linked Equations) scheme as the pressure-velocity coupling algorithm. The laminar flow and species transport models were applied and solved using second order upwind spatial discretization for the steady state solution and first order implicit discretization for the transient order formulation. Convergence of the continuity and velocity equations and the scalar (tracer) was achieved when the steady state and transient state residuals reached 10^{-6} or below. The governing equations for the flow field, assuming isothermal and incompressible Newtonian fluids, were the continuity and Navier-Stokes equations shown in Equation 6 and 7 respectively [50]:

$$\nabla \cdot \boldsymbol{u} = 0 \quad (6)$$

$$\rho \left[\frac{\partial \boldsymbol{u}}{\partial t} + \boldsymbol{u} \cdot \nabla \boldsymbol{u}\right] = -\nabla p + \mu \nabla^2 \boldsymbol{u} \quad (7)$$

where u is the velocity vector, ρ is density, μ is viscosity and t is time. The species concentration distribution was calculated using the convection and diffusion equation shown in Equation 8:

$$\frac{\partial c}{\partial t} + \boldsymbol{u} \cdot \nabla c = D \nabla^2 c \quad (8)$$

where c is the concentration variable and D is diffusion coefficient. Face meshing with quadrilateral elements was applied to produce approximately 500,000 elements in a mapped scheme. The element size was adjusted accordingly for varying D, u and L simulations to maintain mesh independency. A greater density of cells was placed radially compared to the axial direction in order to accurately capture fluid flow along the streamlines and boundary layers. Water was used as the liquid phase in the CFD simulations with temperature dependant physical properties. Initially the steady velocity and momentum equations were solved to establish the velocity flow profile, after which the species equations were solved via a transient approach. Larger time steps were required for decreasing fluid velocities and approximately 1500 – 2000 steps were satisfactory to reach solution convergence. The species transport model treated the tracer fluid as a continuum whose properties were set to be identical to the bulk fluid to reduce any significant effects on the flow field. The step method approach was used to predict the velocity distribution; here we mimicked a step injection of the tracer at the inlet by changing the normalized species concentration from 0 to 1 at the inlet. The area weighted average molar concentration of the species was monitored at the outlet as a function of time.

The boundary condition at the inlet was set by a constant velocity and a constant atmospheric pressure condition was imposed at the outlet. A no-slip condition was applied along the walls of the microchannels and the zero diffusive flux condition was specified at the walls for the tracer species transport equation. The transient simulation was initialized by patching a small region of the inlet with the species to remove the effect of the developing parabolic profile and introduce the tracer uniformly across the cross section. Therefore, the CFD reactor was treated with closed-open boundary conditions as the fluid was introduced with a plug flow velocity profile into the reactor and a radial variation in concentration was observed both during and upstream of the reaction.

2.6. Neutralization reaction

The acid-base neutralization shown in Equation 9 represents a reaction between sodium hydroxide (NaOH) and hydrochloric acid (HCl) to produce sodium chloride and water [51]:

$$HCl + NaOH \rightarrow NaCl + H_2O \quad (9)$$

The NaOH (1M) and HCl (1M) aqueous solutions were each mixed with bromothymol blue indicator in a 40:3 ratio respectively. The MFR, initially empty, was primed with 15 mL of the HCl solution at a flow rate 2 mL/min for the step in. For the washout, 15 mL of the NaOH solution was pumped into the MFR at the same flow rate. This was repeated for flow rates of 3 and 4 mL/min. The sequential (instead of simultaneous) injection of HCl and NaOH solutions through the MFR enabled an assessment of the extent of backmixing within the microcapillaries in the presence of a chemical reaction from the transient response, instead of relying solely on the steady-state extent of conversion.

2.7. 4th Bourne reaction

The 4th Bourne reaction is a well-established reaction used for assessing the extent of micromixing in chemical reactors [13]. It is composed of a set of competing reactions between the neutralization of HCl and NaOH (Equation 10) and the hydrolysis of DMP (Equation 11) to form acetone (CH_3COCH_3) and methanol (CH_3OH) [52]:

$$HCl + NaOH \xrightarrow{k_1} NaCl + H_2O \qquad k_1 = 1.3 \times 10^{11} \frac{m^3}{(kmol \cdot s)} \quad @\ 25°C \quad (10)$$

$$DMP + H_2O \xrightarrow{H^+, k_2} CH_3COCH_3 + 2 \cdot CH_3OH \qquad k_2 = 700 \frac{m^3}{(kmol \cdot s)} \quad @\ 25°C \quad (11)$$

The kinetics of the hydrolysis of DMP are defined by Equation 12:

$$r_c = -kC_{DMP}C_{H^+} \quad (12)$$

This means that in an ideal 'instantaneous' micromixer, the neutralisation of HCl and NaOH happens very quickly and therefore no acetone is formed, yet in a 'real' reactor uneven or slow mixing results in the production of acetone, from which the degree or quality of micromixing can be assessed. Two aqueous feed solutions were prepared for the reaction, a main feed composed of 200 mol/cm^3 DMP, 210 mol/cm^3 NaOH (prepared from pellets), 100 mol/cm^3 NaCl and 254 mol/cm^3 ethanol and a side feed composed of 2000 mol/cm^3 of HCl (prepared from a 5M HCl stock solution) and 529 mol/cm^3 ethanol. The volumetric flow ratio of the main feed to side feed was kept constant at 10:1. The reaction was initiated as 50 mL of the main feed was pumped into the MFR at 2 mL/min and 5 mL of the side feed at 0.2 mL/min. The MFR outlet collected the product in 2 mL Eppendorf tubes pre-loaded with 1.5 mL of 5M sodium hydroxide quenching agent. Product samples (0.5 mL) of the reaction mixture were collected every minute and shaken vigorously. The samples were analysed in a UV spectrophotometer (Cary 100, Agilent) to measure the conversion of acetone at an absorbance value of 265 nm over 25 minutes.

2.8. Image analysis

Digital RGB images of breakthrough curves in the tubular reactors were split into red, green and blue channels with the ImageJ software (NIH, USA). Using the green channel for the maximum signal-to-noise ratio, absorbance values were calculated based on the grey scale peak height and averaged across the 10 capillaries (Equation 13), as previously reported in our group for colorimetric immunoassays [53], [54]:

$$Abs = -log_{10}\left(\frac{I}{I_0}\right) \quad (13)$$

where I is the grey scale peak height and I_0 is the background grey scale value.

3. Results and discussion

3.1. Transition from convective flow to plug flow is linked to molecular diffusion

By experimentally imaging tracing breakthrough experiments, we noticed the concentration of the dyed tracer in narrow capillaries was consistent radially, clearly deviating from ideal plug flow towards convective parabolic flow as D increased from ~400 to 2,400 μm (Figure 1a). This matched the CFD simulations, displaying sharper C/C_0 profiles and greater radial dispersion for small D (Figure 1b). The CFD simulations were carried out for a single-phase fluid, whose optimal grid resolution was determined using the maximum fluid velocity in a mesh independency study summarised in Figure 1e. We noticed the breakthrough of the tracer happened at a normalized flow time around 1 for diffusive species with larger D_m =10^{-6} m^2/s or θ=0.5 for species with small D_m = 10^{-9} m^2/s, which is consistent with near-ideal plug flow and convective flow conditions respectively (Figure 1c). Though convective flow dominates flow hydrodynamics at low D_m, we noticed greater radial dispersion over time for the narrow microcapillary as a result of the smaller distance and shorter diffusion times. The trends above were remarkably similar to experimental concentration profiles illustrating flat radial velocity profiles (inferring plug flow behaviour) in the microcapillary and fully developed parabolic profiles for the meso-capillary with D=2,400 μm (Figure 1d). Note that the capillary with D=1,100 μm displayed slightly convective behaviour initially (θ~0.4) and over time ($\theta \geq 1.25$) exhibited near plug flow characteristics as radial diffusive forces dominated over time. This is to our understanding the first numerical and experimental demonstration of the transition from convective, laminar flow to plug flow, for a chemical species, which happens solely by the role of molecular diffusion. Furthermore, we estimate using Hagen-Pouiselle ($\Delta P=128L\mu Q/\pi D^4$) [55], for volumetric flow rate, Q, that for our flow conditions (L=7 m, 1.5 mL/min), ΔP for the

microcapillary with D=~400 μm was 2.8 bar (0.4 bar/m) and not significantly higher than 0.05 bar (0.007 bar/m) for the meso-capillary (D=1,100 μm). Whereas in meso- and macro-scale tubular chemical systems mixing is essential, unsurprisingly in small scale flow systems and in particular narrow microcapillaries, a good degree of radial mixing with comparable $\Delta P/L$ can be achieved solely by molecular diffusion without the need of complex mixing microstructures.

3.2. Fluid flow profiles in microreactors

We further characterised the fluid hydrodynamic behaviour in the tubular systems using both CFD and experimental breakthrough curves (by monitoring the step input and washout of a dye tracer), allowing comparison of the coiled small (i.d. 1,100 μm) and large (i.d. 2,400 μm) single bore capillary reactors with the 400 μm,10-bore MFR (presented here for the first time). As expected, cumulative F(θ)-curves for the tracer in the smallest D capillaries predominantly showed characteristics of near-ideal plug flow. In the particular case of the MFR, we further observed slightly narrower RTD in the middle capillaries (capillary 4-7, slightly wider) compared to the outer capillaries, as a result of a small variation in the inner D which is an intrinsic effect of the continuous manufacturing process for the fabrication of microcapillary film material (Figure 2a) [56]. The mean hydraulic diameters as measured for the individual capillaries in the microcapillary film are presented in Figure S2 in the supplementary material, from which we expect larger D capillaries will have slightly higher superficial flow velocities and larger flow rates. Although our data imaging technique allowed individual interrogation of microcapillaries, in this study we considered variations in inner diameter to be an intrinsic feature of the material (deriving from the melt-extrusion process) and therefore we focused on analysing the combined (10-bore mean) breakthrough responses. The maldistribution of flow in microcapillary film materials with different bore diameters was previously acknowledged in a study by Reis and Puma (2015), highlighting that small variations in the internal diameter

(and consequently pressure drop) can have a significant variation on the mean residence time [56]. Studying both the step input and washout F-curves, we estimated D_{ax}/uL values in the range of 0.0040-0.0045, meaning near ideal plug flow behaviour with small extents of axial dispersion; note ideal plug flow is usually accepted for $D_{ax}/uL < 0.01$ [46]. As D increased from ~400 to 1,100 μm, we observed deviations from plug flow and a higher D_{ax}/uL value of 0.009 resulting from longer diffusion distances/times (Figure 2b). Convective forces dominated as D increased further to 2,400 μm in the single-large bore capillary, matching closely to the typical 'laminar' model which has a very broad RTD due to slow moving fluid elements near the wall, being also characterised by a long tail (Figure 2c). We believe the diminished hydrodynamic performance obtained with the large D offsets the advantages of large sample volume and lower ΔP, whereas tight residence times in the small D correlate directly with improved product formation via well-controlled reaction kinetics.

For the sake of computational time and effort, the CFD simulated breakthrough curve for D=400 μm was carried out in a mesh with just 10% of the length of the capillaries (called here the scale down mesh). In Figure 2a we demonstrate the D_{ax}/uL obtained experimentally for a 7.4 m full-length capillary (0.0045) fairly matched the D_{ax}/uL value obtained with the scale down mesh (0.067*0.1=0.0067). We found good agreement between experimental data and CFD results using the scaled down D_{ax}/uL values. Our CFD simulations covering the full reactor length (1.7 m) for the larger 2,400 μm capillary also agreed well with experimental RTD data, stating that convective, segregated forces dominate in large D (Figure 2c). It should be noted that our CFD simulations did not account for Dean forces experienced in the coiled reactors which may have led to minor discrepancies. This would potentially lead to a narrower RTD due to additional centrifugal forces for very small coiled diameters [57]. We estimated the Dean number using the curvature radius R, via $Re\sqrt{(D/2R)}$ [58], at the flow rate we tested (1.5 mL/min) to be low at 3.04 and 2.05 for the small bore and large bore reactor respectively.

The aluminium casing for the MFR had curvature R values varying between 0.015 and 0.023 m, from which we estimated that Dean numbers remaining below 10. Therefore, the strength of secondary flows in our different microreactor configurations would be minimal.

3.3. Tuning the RTD by varying design and molecular parameters

We used the validated CFD model to determine the impact of design and molecular parameters on the RTD, hence improving the performance of the tubular flow reactors. For species presenting D_m in the range of 10^{-4}-10^{-7} m^2/s (covering most common chemical transformations in single phase flow systems), the E(θ)-curves showed the fluid approaching near-ideal plug flow for narrower capillaries and mostly convective flow for larger bore capillaries (Figure 3a). D_m describes the extent of molecular flux in the direction of the concentration gradient, therefore a higher D_m significantly pronounces the diffusive drive towards near-ideal plug flow (Figure 3a). Diffusion of molecules in liquid solutions are inherently slow compared to gaseous systems, with the typical range of chemicals, dyes, proteins and bacteria lying within the range of 10^{-11} to 10^{-9} m^2/s [28]–[32]. Therefore, the use of small D, especially in liquid reagents with poor 'interfacial' mixing, would significantly benefit reactors by reducing the diffusion distance for a direct impact on improved radial mixing and reaction conversion rates.

The residence time is directly linked to the mean superficial fluid velocity and length of capillary, both important factors in scaling-up chemical reactions in a tubular reactor. For all diameters we observed that the RTD broadened as the velocity increased (Figure 3b) and the length decreased (Figure 3c) as axial spreading reduced, translating to more uneven processing times for individual molecules in chemical reactions that may result in a reduction of conversion and selectivity.

For all scenarios of D_m, L and u studied, it becomes evident that the RTD in large D capillaries is highly sensitive to changes in the system compared to narrower microcapillaries which

interestingly, remained predominantly plug flow. Our simulations were in excellent agreement with experimental velocity studies, showing minimal deviations from plug flow under varying flow rates in the MFR (see Figures S3a-b in supplementary material).

3.4. Effect of Reynolds number on axial dispersion

We plotted CFD and experimental axial dispersion results in the format of Taylor-Aris dispersion plots which superimpose the axial dispersion model and molecular diffusion effects. These plots infer that higher *Re* will lie in the right region of the plot dominated by convection, lowering *Re* shifts towards the left region where dispersion is influenced greatly by diffusion, whilst the minimum D_{ax}/ud value expresses ideal plug flow. Our CFD simulations, lying on the 0.1 mm^2/s theoretical line, support these trends and demonstrate that over the same mean fluid velocity range, dispersive effects diminish as *D* is decreased (Figure 4a).

The step input / washout experimental technique allowed us to fairly approximate the closed-open boundary condition of the CFD simulation by introducing the tracer at the inlet as plug flow (Figure S4). Experimental data for the 400 µm and 1,100 µm capillary lies on theoretical models with D_m ranging from $5x10^{-10}$ to $2x10^{-9}$ m^2/s (0.0005-0.002 mm^2/s) and discrepancies in data, for example D_{ax}/ud values of 50.8 ± 10.5 at 0.015 m/s, for the MFR arising presumably from the maldistribution of flow between the ten parallel microcapillaries [59] (Figure 4b). Many data points for the small-bore capillary lie on the 10^{-9} m^2/s model, matching the value of D_m for the tracer dye (~10^{-9} m^2/s) [60].

Concurring with our CFD simulations, capillaries with large *D* had high D_{ax}/ud values ranging 29-106 within velocity range 0.008-0.087 m/s, comparatively small *D* had lower D_{ax}/ud values of 18-69 over approximately the same velocity range. This is a clear indication that small *D* capillaries present fluid hydrodynamics closer to ideal plug flow, which isfurther supported by data in Table 1 showing low D_{ax}/uL values for individual microcapillaries in the MFR ranging

from 0.0015±0.0005 to 0.0033±0.0006 for flow rates of 0.5 to 5.0 mL/min. Although there was a significant spread (around 36% for flow rates up to 1 mL/min) of D_{ax}/uL values due to the non-uniform flow distribution in the MFR, D_{ax}/uL for individual capillaries were smaller than the average across all 10 capillaries (data not shown). Surprisingly we found D_{ax}/uL in the individual microcapillaries remained mostly constant for $9<Re<44$, with D_{ax}/uL values ranging within 0.006-0.014 (Figure 4c). This suggests that the molecular diffusive effects across the short diffusion distance of the microcapillaries are sufficient to overcome the increased axial dispersion from the higher velocities.On the contrary, the larger single bore capillary presented a clear and stable trend of increasing axial dispersion as *Re* increased. This shows that flow characteristics in narrow capillaries remain mostly independent of the flow conditions and the same does not stand true for larger bore reactors, indicating that meso-scale tubular reactors are not linearly scalable.

3.5. Transition region for flow in tubular microcapillaries

Our combined experimental RTD and CFD simulation results suggested the transition of concentration profiles from convective flow to near plug flow is dependent on D_m but also on the scale of the system, in particular D and L. These relationships have not yet been fully established in literature. In the absence of secondary flow, the concentration profile "dissociates" from the parabolic velocity profile through the role D_m. By being a scalar, D_m promotes the movement of fluid molecules in both radial and axial directions, helping to homogenise the concentration profile radially and produce the desirable near plug-flow concentration profile. It allows smoothing the concentration in the streamlines closer to the centre of the capillary and reducing the tailing caused by stagnant fluid elements closer to the wall (due to non-slip wall).

We hypothesised the transition from convective to near plug flow is linked to the time scales of convection and diffusion. To validate that, we defined a convective time, $t_{conv} = L/u$ and a diffusive time, $t_{diff} = D^2/8D_m$, with the last based on Einstein's law of molecular diffusion (with maximum diffusion distance being half the diameter of the capillary - more details provided in the Supplementary Information file). Depending on the value of D_m, multiple outcomes are expected in terms of outlet concentration profile, these have been schematically captured in Figure 5a.

In the absence of D_m or when this is negligible, the concentration profile is mostly dictated by the parabolic velocity profile, therefore with breakthrough curves approaching that for a pure convective system. On the other extreme, when D_m is too large, t_{diff} is very short which means very fast radial mixing but also higher axial dispersion as molecules can diffuse quickly both radially and axially. It is know that for a 'pure' convective system, a sharp rise in concentration happens for half the mean residence time (i.e. $\theta = 0.5$, in terms of E-curve) or for the ideal plug flow for $\theta = 1$ (in terms of F-curve). In Figure 5b we have summarised the breakthrough time, θ_b, at which a significant increase in concentration could be detected from our CFD simulations and we colour-mapped the array according to where it stands in respect to a transition, cut-off value of $\theta_B = 0.75$ (assumed as the quantitative parameter for the transition). A value larger than 0.75 means flow approached plug flow and less than 0.75 means a high degree of segregation and therefore flow mostly convective. For a capillary with D=400 µm, the concentration profile remained close to plug flow (with $\Theta_B = 0.8\text{-}0.9$) over varying D_m, u and L parameters, with the exception of very short capillaries and very large D_m, and with D increasing Θ_B decreased for all cases so that flow transitioned away from plug flow.

We observed from the colour maps that Θ_B (and therefore flow transition) is linked to the absolute value for t_{diff} and t_{conv} and also the ratio t_{diff}/t_{conv} (see supplementary methods for

equations) and based on the limited number of experimental combinations tested, we have identified a critical value for t_{diff}/t_{conv} ~ 0.15 for that transition. Larger i.d. capillaries and small D_m values are known to produce a convective flow, this actually translates into large t_{diff} values compared to t_{conv} and therefore large t_{diff}/t_{conv} ratios.

We also observed that depending on the D_m value of the species, there is a linear semi-log relationship between D and t_{diff} (Figure 5c(i)) and t_{diff}/t_{conv} (Figure 5c(ii)) and that flow is in general plug flow for t_{diff}/t_{conv} values smaller than 0.15. It is also possible to obtain from Figure 5c(i) information about the critical diameter of the system. For example, with a D_m of 10^{-7} m^2/s the largest D that could be used for near plug flow is 800-900 μm (resulting from the interception of the red horizontal line with the data series for constant D_m), confirming the need to use sub-millimetre systems in continuous reactive flows. In general, t_{diff}/t_{conv} values less than 0.15 produced near plug flow, yet these appeared restrained by other flow conditions. For example, when the superficial flow velocity is too small (and therefore t_{conv} large) or D_m is too large (and therefore t_{diff} is small), flow is highly dispersed due to enhanced D_m or axial dispersion, which actually agrees with the core concept of the Aris-Taylor plot. Figure 5c(iii) summarises the relationship of t_{diff}/t_{conv} vs D as a flow map, demonstrating graphically that near plug flow only happens for a narrow window of D and molecular and flow conditions with transitions to dispersive and convective flow. Note that a greater number of data points will be required to increase the accuracy of the plug flow region and critical t_{diff}/t_{conv} value.

3.6. Continuous flow reactions in the MFR

We have demonstrated the advantages of utilising sub-millimetre capillaries as advanced continuous tubular reactors by carrying out two flow reactions in the multiplexed MFR, these being a neutralization reaction and an acid-catalysed hydrolysis (4th Bourne) reaction [51]. Main results are summarised in Figure 6.

Our sequential neutralization reaction used bromothymol blue indicator on both NaOH and HCl solutions which produced colorimetric changes in accordance with the solution pH in order to observe reaction kinetics. A reaction flowing a yellow acidic HCl through the MFR, followed by a dark blue alkaline NaOH produced a neutral NaCl product with a green colour. The reaction has a very high reaction rate constant of 1.3×10^{11} $m^3/(kmol \cdot s)$ [52], indicating that non-ideal micromixing and any minor deviations from plug flow should reflect a large effect on the reaction rate. Plug flow conditions should induce a sharp peak when the reaction is initiated in the small *D* capillary, whereas we expect a gradual increase in absorbance in a large *D* capillary with dominant convective effects (Figure 6a). We noticed sharp peaks for our reactions in individual capillaries within the MFR at 2 mL/min and as supported by visual observations, larger middle capillaries (4-7) breaking through first as expected (Figure 6b),again this is linked to the small variations on the *D* of the microcapillaries deriving from the manufacturing process [61]. As the neutralization reaction progressed and the pH shifted towards neutral, the absorbance declined over time until a plateau was reached.

The peak times for the sequential neutralisation correlated well with both the mean residence time determined from the experimental RTD curves (Figure 6c) and the mean hydraulic time (Figure S5a) for the range of flow rates testes (2-4 mL/min), confirming the reactive system in the microcapillaries behaved as plug flow as the reaction progressed. In addition, we observed the peak absorbances for each individual capillary were smaller and almost coincident for the flow rates of 2 and 3 mL/min and 20-80% larger for flow rate of 4 mL/min, suggesting micromixing is more effective at smaller flow rates, presumably due to extended time for the reactions (Figure S5b). Note the absorbance peaks in the sequential neutralisation reaction are linked to the intense blue colour of the NaOH solution with an indicator, which can only be seen when the mixing of HCl with NaOH is not instantaneous, therefore higher peak heights mean increased axial spreading.

The 4th Bourne reaction is a set of competing reactions between the neutralization of NaOH and HCl and the hydrolysis of DMP to produce acetone and methanol and it is therefore used as a model reaction for characterising micromixing in tubular reaction systems. The formation of products is a valuable indication of the level of mixing in a (micro)reactor, such that hydrolysis of DMP will not be observed and no acetone will be present in perfect mixing conditions (Figure 6d). We compared the transient response of a pure 2M acetone solution in the MFR with the production of acetone in the 4th Bourne reaction. We observed low acetone conversion (around 21%) in the MFR for 0.2 M DMP at 2 mL/min which indicated instantaneous excellent mixing and a very fast neutralisation reaction, this fast radial mixing was further supported with cumulative F-curves for pure acetone showing plug flow behaviour (Figure 6e). By studying transient DMP conversion for a range of flow rates (1.0-2.5 mL/min) we find no discernible trend (Figure 6f), confirming that the chemical and fluid characteristics remain similar with increasing *Re* as reported in section 3.4. In Figure 6f we best-fitted transient acetone production in the reactive system with the hydrodynamic model for plug flow with axial dispersion as shown in equation 4.From this, we noticed very low D_{ax}/uL values (in the range of 0.012-0.030) with no clear link to the flow rates tested, meaning high reaction performance mostly independent of *Re* or mean residence time.

In line with our experimental tracer breakthrough curves and CFD simulations, both 'sequential' neutralisation reaction and 'parallel' 4th Bourne reaction in the MFR demonstrate good performance with fast radial mixing under varying design parameters, highlighting the scalability and high-end performance of the system. In particular, the 10-bore parallel small *D* capillaries offer capabilities of scaling up the reaction volume without compromising high conversions and yields, in contrast to the meso-scale capillaries. A multitude of additional reactions may be performed in the MFR as the Teflon® FEP material provides excellent chemical resilience. Furthermore, a range of temperature dependant reactions may be

accommodated using the aluminium alloy casing which provides uniform heat transfer along the MFR length with the use of a compact oven.

4. Conclusions

This is to our understanding one of the first reports of the transition from convective, segregated flow to plug flow being numerically and experimentally captured in a tubular system. CFD studies validated with fluid tracing and continuous flow chemistry reactions demonstrated the strong influence of D and D_m on reagents dispersion and chemical conversion. The transition between convective flow, plug flow and dispersed flow correlated well with the ratio between the intrinsic time scales for diffusion and convection, given by a new parameter t_{diff}/t_{conv} which complements insights from Aris-Tylor plot yet making transition fully quantitative and scalable.

Highly consistent under varying flow conditions, the small D exhibited excellent radial mixing with low $D_{ax}/uL < 0.01$ whilst the large D shifted towards very dispersive flow at high *Re.* Experimental data for the single bore 1100 μm capillary matched the expectation from the Taylor-Aris dispersion plot, fitting well with the 10^{-9} m^2/s theoretical line. The MFR is uniquely capable of combining the best of two worlds; relevant V and small ΔP, both typical of meso-reactors, with optimized plug flow distinctive of small-bore systems. We envisage full potential of sub-millimetre flow reactors like the MFR by scaling up reaction volume through parallelization of flow in the multi-bore flow technology.

Acknowledgements

K.K. Gill is grateful to EPSRC and University of Bath for financial support through funding a Ph.D. scholarship. The authors are grateful to anonymous reviewer number 3, for challenging

us to present a critical diameter for the transition, which has inspired us to develop the colour maps and the dimensionless parameter for the transition, t_{diff}/t_{conv}.

References

[1] W. Xu, Y. Su, M. Shang, X. Lu, and Q. Lu, "Rapid synthesis of polyimide precursors by solution polymerization using Continuous-flow microreactors," *Chem. Eng. J.*, vol. 397, no. April, p. 125361, 2020, doi: 10.1016/j.cej.2020.125361.

[2] M. Baumann, T. S. Moody, M. Smyth, and S. Wharry, "A Perspective on Continuous Flow Chemistry in the Pharmaceutical Industry," *Org. Process Res. Dev.*, 2020, doi: 10.1021/acs.oprd.9b00524.

[3] P. Plouffe, A. Macchi, and D. M. Roberge, "From batch to continuous chemical synthesis-a toolbox approach," *Org. Process Res. Dev.*, vol. 18, no. 11, pp. 1286–1294, 2014, doi: 10.1021/op5001918.

[4] P. W. Miller, N. J. Long, A. J. De Mello, R. Vilar, H. Audrain, D. Bender, J. Passchier, and A. Gee, "Rapid multiphase carbonylation reactions by using a microtube reactor: Applications in positron emission tomography 11C-radiolabeling," *Angew. Chemie - Int. Ed.*, vol. 46, no. 16, pp. 2875–2878, 2007, doi: 10.1002/anie.200604541.

[5] L. J. Martin, A. L. Marzinzik, S. V. Ley, and I. R. Baxendale, "Safe and reliable synthesis of diazoketones and quinoxalines in a continuous flow reactor," *Org. Lett.*, vol. 13, no. 2, pp. 320–323, 2011, doi: 10.1021/ol1027927.

[6] H. Löwe, V. Hessel, P. Lob, and S. Hubbard, "Addition of secondary amines to α,β-unsaturated carbonyl compounds and nitrites by using microstructured reactors," *Org. Process Res. Dev.*, vol. 10, no. 6, pp. 1144–1152, 2006, doi: 10.1021/op0501949.

[7] M. Escribà, V. Hessel, S. Rothstock, J. Eras, R. Canela, and P. Löb, "Applying a continuous capillary-based process to the synthesis of 3-chloro-2-hydroxypropyl pivaloate," *Green Chem.*, vol. 13, no. 7, pp. 1799–1805, 2011, doi: 10.1039/c0gc00655f.

[8] M. Brzozowski, M. O'Brien, S. V. Ley, and A. Polyzos, "Flow chemistry: Intelligent processing of gas-liquid transformations using a tube-in-tube reactor," *Acc. Chem. Res.*, vol. 48, no. 2, pp. 349–362, 2015, doi: 10.1021/ar500359m.

[9] A. J. Blacker and K. E. Jolley, "Continuous formation of N-chloro-N,N-dialkylamine solutions in well-mixed meso-scale flow reactors," *Beilstein J. Org. Chem.*, vol. 11, pp. 2408–2417, 2015, doi: 10.3762/bjoc.11.262.

[10] K. Robertson, "Using flow technologies to direct the synthesis and assembly of materials in solution," *Chem. Cent. J.*, vol. 11, no. 1, pp. 1–18, 2017, doi: 10.1186/s13065-016-0229-1.

[11] J. Wegner, S. Ceylan, and A. Kirschning, "Ten key issues in modern flow chemistry," *Chem. Commun.*, vol. 47, no. 16, pp. 4583–4592, 2011, doi: 10.1039/c0cc05060a.

[12] V. Hessel, D. Kralisch, N. Kockmann, T. Noël, and Q. Wang, "Novel process windows for enabling, accelerating, and uplifting flow chemistry," *ChemSusChem*, vol. 6, no. 5, pp. 746–789, 2013, doi: 10.1002/cssc.201200766.

[13] J. R. Bourne, "Mixing and the selectivity of chemical reactions," *Org. Process Res. Dev.*, vol. 7, no. 4, pp. 471–508, 2003, doi: 10.1021/op020074q.

[14] S. Schwolow, J. Hollmann, B. Schenkel, and T. Röder, "Application-oriented analysis of mixing performance in microreactors," *Org. Process Res. Dev.*, vol. 16, no. 9, pp. 1513–1522, 2012, doi: 10.1021/op300107z.

[15] M. O. Coppens, "Scaling-up and -down in a nature-inspired way," *Ind. Eng. Chem. Res.*,

vol. 44, no. 14, pp. 5011–5019, 2005, doi: 10.1021/ie0490482.

[16] S. R. L. Gobert, S. Kuhn, L. Braeken, and L. C. J. Thomassen, "Characterization of Milli- and Microflow Reactors: Mixing Efficiency and Residence Time Distribution," *Org. Process Res. Dev.*, vol. 21, no. 4, pp. 531–542, 2017, doi: 10.1021/acs.oprd.6b00359.

[17] N. Kockmann, M. Gottsponer, and D. M. Roberge, "Scale-up concept of single-channel microreactors from process development to industrial production," *Chem. Eng. J.*, vol. 167, no. 2–3, pp. 718–726, 2011, doi: 10.1016/j.cej.2010.08.089.

[18] A. Mariotti, M. Antognoli, C. Galletti, R. Mauri, M. V. Salvetti, and E. Brunazzi, "The role of flow features and chemical kinetics on the reaction yield in a T-shaped micro-reactor," *Chem. Eng. J.*, vol. 396, no. April, p. 125223, 2020, doi: 10.1016/j.cej.2020.125223.

[19] D. M. Roberge, L. Ducry, N. Bieler, P. Cretton, and B. Zimmermann, "Microreactor technology: A revolution for the fine chemical and pharmaceutical industries?," *Chem. Eng. Technol.*, vol. 28, no. 3, pp. 318–323, 2005, doi: 10.1002/ceat.200407128.

[20] S. K. Kurt, M. G. Gelhausen, and N. Kockmann, "Axial Dispersion and Heat Transfer in a Milli/Microstructured Coiled Flow Inverter for Narrow Residence Time Distribution at Laminar Flow," *Chem. Eng. Technol.*, vol. 38, no. 7, pp. 1122–1130, 2015, doi: 10.1002/ceat.201400515.

[21] J. Yue, "Multiphase flow processing in microreactors combined with heterogeneous catalysis for efficient and sustainable chemical synthesis," *Catal. Today*, vol. 308, no. September 2017, pp. 3–19, 2018, doi: 10.1016/j.cattod.2017.09.041.

[22] B. Ahmed-Omer, J. C. Brandt, and T. Wirth, "Advanced organic synthesis using

microreactor technology," *Org. Biomol. Chem.*, vol. 5, no. 5, pp. 733–740, 2007, doi: 10.1039/b615072a.

[23] A. Nagaki, M. Togai, S. Suga, N. Aoki, K. Mae, and J. I. Yoshida, "Control of extremely fast competitive consecutive reactions using micromixing. Selective Friedel-Crafts aminoalkylation," *J. Am. Chem. Soc.*, vol. 127, no. 33, pp. 11666–11675, 2005, doi: 10.1021/ja0527424.

[24] H. Shi, Y. Zhao, and Z. Liu, "Numerical investigation of the secondary flow effect of lateral structure of micromixing channel on laminar flow," *Sensors Actuators, B Chem.*, vol. 321, no. February, 2020, doi: 10.1016/j.snb.2020.128503.

[25] H. Shi, K. Nie, B. Dong, L. Chao, F. Gao, M. Ma, M. Long, and Z. Liu, "Mixing enhancement via a serpentine micromixer for real-time activation of carboxyl," *Chem. Eng. J.*, vol. 392, no. October 2019, p. 123642, 2020, doi: 10.1016/j.cej.2019.123642.

[26] X. Nguyen, A. Carafa, and C. H. Hornung, "Hydrogenation of vinyl acetate using a continuous flow tubular reactor with catalytic static mixers," *Chem. Eng. Process. Process Intensif.*, vol. 124, no. December 2017, pp. 215–221, 2018, doi: 10.1016/j.cep.2017.12.007.

[27] S. I. A. Shah, L. W. Kostiuk, and S. M. Kresta, "The effects of mixing, reaction rates, and stoichiometry on yield for mixing sensitive reactions - Part I: Model development," *Int. J. Chem. Eng.*, vol. 2012, 2012, doi: 10.1155/2012/750162.

[28] D. Bošković and S. Loebbecke, "Modelling of the residence time distribution in micromixers," *Chem. Eng. J.*, vol. 135, no. SUPPL. 1, pp. 138–146, 2008, doi: 10.1016/j.cej.2007.07.058.

[29] L. Hohmann, M. Schmalenberg, M. Prasanna, M. Matuschek, and N. Kockmann,

"Suspension flow behavior and particle residence time distribution in helical tube devices," *Chem. Eng. J.*, vol. 360, no. October 2018, pp. 1371–1389, 2019, doi: 10.1016/j.cej.2018.10.166.

[30] Y. Huang, M. M. Coggon, R. Zhao, H. Lignell, M. U. Bauer, R. C. Flagan, and J. H. Seinfeld, "The Caltech Photooxidation Flow Tube reactor: Design, fluid dynamics and characterization," *Atmos. Meas. Tech.*, vol. 10, no. 3, pp. 839–867, 2017, doi: 10.5194/amt-10-839-2017.

[31] A. M. Nightingale, J. H. Bannock, S. H. Krishnadasan, F. T. F. O'Mahony, S. A. Haque, J. Sloan, C. Drury, R. McIntyre, and J. C. Demello, "Large-scale synthesis of nanocrystals in a multichannel droplet reactor," *J. Mater. Chem. A*, vol. 1, no. 12, pp. 4067–4076, 2013, doi: 10.1039/c3ta10458c.

[32] J. H. Bannock, S. H. Krishnadasan, A. M. Nightingale, C. P. Yau, K. Khaw, D. Burkitt, J. J. M. Halls, M. Heeney, and J. C. De Mello, "Continuous synthesis of device-grade semiconducting polymers in droplet-based microreactors," *Adv. Funct. Mater.*, vol. 23, no. 17, pp. 2123–2129, 2013, doi: 10.1002/adfm.201203014.

[33] A. Laybourn, A. M. López-Fernández, I. Thomas-Hillman, J. Katrib, W. Lewis, C. Dodds, A. P. Harvey, and S. W. Kingman, "Combining continuous flow oscillatory baffled reactors and microwave heating: Process intensification and accelerated synthesis of metal-organic frameworks," *Chem. Eng. J.*, vol. 356, no. May 2018, pp. 170–177, 2019, doi: 10.1016/j.cej.2018.09.011.

[34] V. C. Eze, J. C. Fisher, A. N. Phan, and A. P. Harvey, "Intensification of carboxylic acid esterification using a solid catalyst in a mesoscale oscillatory baffled reactor platform," *Chem. Eng. J.*, vol. 322, pp. 205–214, 2017, doi: 10.1016/j.cej.2017.04.038.

[35] A. N. Phan and A. Harvey, "Development and evaluation of novel designs of continuous

mesoscale oscillatory baffled reactors," *Chem. Eng. J.*, vol. 159, no. 1–3, pp. 212–219, 2010, doi: 10.1016/j.cej.2010.02.059.

[36] F. R. Mohd Rasdi, A. N. Phan, and A. P. Harvey, "Rapid determination of reaction order and rate constants of an imine synthesis reaction using a mesoscale oscillatory baffled reactor," *Chem. Eng. J.*, vol. 222, pp. 282–291, 2013, doi: 10.1016/j.cej.2013.02.080.

[37] M. C. Rehbein, J. Wolters, C. Kunick, and S. Scholl, "Continuous high-pressure operation of a pharmaceutically relevant Krapcho dealkoxycarbonylation reaction," *J. Flow Chem.*, vol. 9, no. 2, pp. 123–131, 2019, doi: 10.1007/s41981-019-00031-2.

[38] S. Schwolow, B. Heikenwälder, L. Abahmane, N. Kockmann, and T. Röder, "Kinetic and scale-up investigations of a michael addition in microreactors," *Org. Process Res. Dev.*, vol. 18, no. 11, pp. 1535–1544, 2014, doi: 10.1021/op5002758.

[39] M. H. Reis, T. P. Varner, and F. A. Leibfarth, "The Influence of Residence Time Distribution on Continuous-Flow Polymerization," *Macromolecules*, vol. 52, no. 9, pp. 3551–3557, 2019, doi: 10.1021/acs.macromol.9b00454.

[40] A. Cantu-Perez, S. Barrass, and A. Gavriilidis, "Hydrodynamics and reaction studies in a layered herringbone channel," *Chem. Eng. J.*, vol. 167, no. 2–3, pp. 657–665, 2011, doi: 10.1016/j.cej.2010.10.044.

[41] B. Hallmark, F. Gadala-Maria, and M. R. Mackley, "The melt processing of polymer microcapillary film (MCF)," *J. Nonnewton. Fluid Mech.*, vol. 128, no. 2–3, pp. 83–98, 2005, doi: 10.1016/j.jnnfm.2005.03.013.

[42] C. H. Hornung, B. Hallmark, M. Baumann, I. R. Baxendale, S. V. Ley, P. Hester, P. Clayton, and M. R. MacKley, "Multiple microcapillary reactor for organic synthesis," *Ind. Eng. Chem. Res.*, vol. 49, no. 10, pp. 4576–4582, 2010, doi: 10.1021/ie901674h.

[43] N. M. Reis, J. Pivetal, A. L. Loo-Zazueta, J. M. S. Barros, and A. D. Edwards, "Lab on a stick: Multi-analyte cellular assays in a microfluidic dipstick," *Lab Chip*, vol. 16, no. 15, pp. 2891–2899, 2016, doi: 10.1039/c6lc00332j.

[44] C. H. Hornung, M. R. Mackley, I. R. Baxendale, and S. V Ley, "A Microcapillary Flow Disc Reactor for Organic Synthesis," vol. 11, no. 3, pp. 399–405, 2007, doi: 10.1021/op700015f.

[45] C. H. Hornung and M. R. Mackley, "The measurement and characterisation of residence time distributions for laminar liquid flow in plastic microcapillary arrays," vol. 64, pp. 3889–3902, 2009, doi: 10.1016/j.ces.2009.05.033.

[46] O. Levenspeil, *Chemical Reaction Engineering*. New York: Wiley, 1999.

[47] O. Levenspeil and W. K. Smith, "Notes on the diffusion-type model for longitudinal mixing in flow," *Chem. Eng. Sci.*, vol. 6, pp. 227–233, 1957, doi: 10.1016/0009-2509(60)90008-7.

[48] G. Taylor, "Dispersion of soluble matter in solvent flowing slowly through a tube," *Proc. R. Soc. London. Ser. A. Math. Phys. Sci.*, vol. 219, no. 1137, pp. 186–203, 1953, doi: 10.1098/rspa.1953.0139.

[49] N. Reis, A. P. Harvey, M. R. Mackley, A. A. Vicente, and J. A. Teixeira, "Fluid mechanics and design aspects of a novel oscillatory flow screening mesoreactor," *Chem. Eng. Res. Des.*, vol. 83, no. 4 A, pp. 357–371, 2005, doi: 10.1205/cherd.03401.

[50] ANSYS Inc, "ANSYS Fluent User's Guide, Release 17.2," 2019.

[51] J. Baldyga, J. R. Bourne, and B. Walker, "Non-isothermal micromixing in turbulent liquids: theory and experiment," *Can. J. Chem. Eng.*, vol. 76, no. 3, pp. 641–649, 1998, doi: 10.1002/cjce.5450760336.

[52] R. A. Taylor, W. R. Penney, and H. X. Vo, “Scale-up methods for fast competitive chemical reactions in pipeline mixers,” *Ind. Eng. Chem. Res.*, vol. 44, no. 16, pp. 6095–6102, 2005, doi: 10.1021/ie040237u.

[53] A. I. Barbosa, A. P. Castanheira, A. D. Edwards, and N. M. Reis, “A lab-in-a-briefcase for rapid prostate specific antigen (PSA) screening from whole blood,” *Lab Chip*, vol. 14, no. 16, pp. 2918–2928, 2014, doi: 10.1039/c4lc00464g.

[54] A. I. Barbosa, P. Gehlot, K. Sidapra, A. D. Edwards, and N. M. Reis, “Portable smartphone quantitation of prostate specific antigen (PSA) in a fluoropolymer microfluidic device,” *Biosens. Bioelectron.*, vol. 70, pp. 5–14, 2015, doi: 10.1016/j.bios.2015.03.006.

[55] C. H. Hornung, B. Hallmark, R. P. Hesketh, and M. R. Mackley, “The fluid flow and heat transfer performance of thermoplastic microcapillary films,” no. January, 2006, doi: 10.1088/0960-1317/16/2/030.

[56] N. M. Reis and G. Li Puma, “A novel microfluidic approach for extremely fast and efficient photochemical transformations in fluoropolymer microcapillary films,” *Chem. Commun.*, vol. 51, no. 40, pp. 8414–8417, 2015, doi: 10.1039/c5cc01559f.

[57] S. Klutz, S. K. Kurt, M. Lobedann, and N. Kockmann, “Narrow residence time distribution in tubular reactor concept for Reynolds number range of 10-100,” *Chem. Eng. Res. Des.*, vol. 95, pp. 22–33, 2015, doi: 10.1016/j.cherd.2015.01.003.

[58] N. Nivedita, P. Ligrani, and I. Papautsky, “Dean Flow Dynamics in Low-Aspect Ratio Spiral Microchannels,” *Sci. Rep.*, vol. 7, no. February, pp. 1–10, 2017, doi: 10.1038/srep44072.

[59] A. P. Castanheira, A. I. Barbosa, A. D. Edwards, and N. M. Reis, “Multiplexed

femtomolar quantitation of human cytokines in a fluoropolymer microcapillary film," *Analyst*, vol. 140, no. 16, pp. 5609–5618, 2015, doi: 10.1039/c5an00238a.

[60] N. M. Reis, D. Y. Chirgadze, T. L. Blundell, and M. R. MacKley, "The effect of protein-precipitant interfaces and applied shear on the nucleation and growth of lysozyme crystals," *Acta Crystallogr. Sect. D Biol. Crystallogr.*, vol. 65, no. 11, pp. 1127–1139, 2009, doi: 10.1107/S0907444909031527.

[61] A. D. Edwards, N. M. Reis, N. K. H. Slater, and M. R. MacKley, "A simple device for multiplex ELISA made from melt-extruded plastic microcapillary film," *Lab Chip*, vol. 11, no. 24, pp. 4267–4273, 2011, doi: 10.1039/c0lc00357c.

List of Tables

Table 1: Axial dispersion coefficients, D_{ax}/uL in the 10 individual capillaries for the MFR over a range of flow rates

	Flow rate (mL/min)									
	0.5		**1.0**		**1.5**		**2.0**		**5.0**	
Capillary	***Re***	D_{ax}/uL	***Re***	D_{ax}/uL	***Re***	D_{ax}/uL	***Re***	D_{ax}/uL	***Re***	D_{ax}/uL
1	2.26	0.0021	4.56	0.0029	6.59	0.0033	8.21	0.0031	20.39	0.0026
2	1.86	0.0008	3.39	0.0012	5.48	0.0022	7.14	0.0024	17.38	0.0026
3	2.80	0.0013	5.81	0.0027	8.25	0.0036	9.95	0.0036	23.38	0.0038
4	3.25	0.0015	6.51	0.0026	9.87	0.0043	13.07	0.0032	30.32	0.0038
5	3.31	0.0016	5.58	0.0024	11.58	0.0039	13.52	0.0028	33.26	0.0037
6	4.67	0.0022	9.47	0.0035	13.58	0.0045	15.87	0.0030	37.43	0.0038
7	4.13	0.0021	8.34	0.0030	12.12	0.0040	13.91	0.0030	32.18	0.0039
8	2.96	0.0011	6.15	0.0025	8.61	0.0045	10.42	0.0034	24.46	0.0033
9	2.23	0.0010	4.56	0.0019	6.74	0.0028	8.10	0.0028	19.66	0.0027
10	2.46	0.0012	4.87	0.0025	6.73	0.0029	8.26	0.0030	20.09	0.0028

Figure captions

Figure 1: (a) Tracer dye at the inlet of the (i) ~400 µm, (ii) 1,100 µm and (iii) 2,400 µm capillary diameters. CFD simulation of the normalized tracer concentration (b) along the length of the capillary and (c) at the capillary outlet (0.05 m/s). (d) Experimental radial dispersion plots for a range of normalized times at 1.5 ml/min. (e) Mesh independency studies at the maximum flow velocity for 0.05 m/s flow velocity.

Figure 2: (a) Cross section and holding alloy plate for the 10-bore, 7.4 m long FEP Teflon microcapillary film reactor (i.d. 363±32.2 µm), (b) 7.0 m small single bore reactor (i.d. 1,100 µm) and (c) 1.7 m large single bore reactor (i.d. 2,400 µm) with corresponding cumulative F(Θ) curves. Validation CFD simulations were carried out for the microcapillary film reactor (capillary 6) scaled down to 0.5 m length and for the full length 1.7 m large bore reactor.

Figure 3: Effect of (a) the diffusion coefficients of molecular species (0.05 m/s, 240 mm) (b) velocities (D_m=10^{-7} m^2/s, 240 mm) and (c) capillary lengths (D_m=10^{-7} m^2/s, 0.05 m/s) on the residence time distributions for three different *D* of capillaries.

Figure 4: Axial dispersion plots with (a) simulation and (b) experimental data for the step input of the microcapillary film reactor and the large bore reactor. (c) Axial dispersion coefficients for the microcapillary film reactor and large bore reactor over a range of Reynold numbers.

Figure 5: (a) Schematic illustrating pure convective flow in a tubular capillary with diameter, *D,* via convection time (t_{conv}) and convective flow coupled with diffusion time (t_{diff}) for a range of molecular diffusion coefficients (D_m). (b) Normalized breakthrough time (Θ_B), t_{conv}, t_{diff} and t_{conv}/t_{diff} at varying D_m, fluid velocities (u) and capillary lengths (L) for a range of *D.* Colour map minimum and maximum limits for Θ_B, t_{conv}, t_{diff} *and* t_{conv}/t_{diff} *are* 0.5 – 0.9, 0.48 – 2400, 2E-4 – 0.04 and 4.2E-5 – 0.5 respectively. (c) Relationship between (i) *D* and t_{conv}/t_{diff} (red line indicates critical t_{conv}/t_{diff} value of 0.15) and (ii) *D* and t_{diff} for D_m ranging from 1E-7 – 1E-4

m^2/s. (iii) Flow map for t_{conv}/t_{diff} over a range of D where $\Theta < 0.75$ indicates, via the breakthrough time, that flow is segregated (convective) / dispersed and $\Theta > 0.75$ approaches plug flow**.**

Figure 6: Continuous flow reactions in the 10-bore microcapillary film reactor. (a) Schematic of the sequential neutralization reaction with bromothymol indicator. (b) Neutralization reaction monitored at the outlet shown visually and by analysing the absorbance over time (inset illustrates the peak absorbance for individual microcapillaries). (c) Neutralization reaction breakthrough time measured against the mean residence time and the individual capillaries in the microcapillary film reactor over a range of flow rates. (d) Schematic of the 4th Bourne reaction studying (e) transient breakthrough for pure 2M acetone and conversion of acetone in 4th Bourne reaction using F-curves. (f) F-curve for the 4th Bourne reaction at 1 mL/min and a study on the transient conversion (X), axial dispersion coefficients (D_{ax}/uL) and mean residence times ($\bar{t}$) over a range of flow rates.

Figures

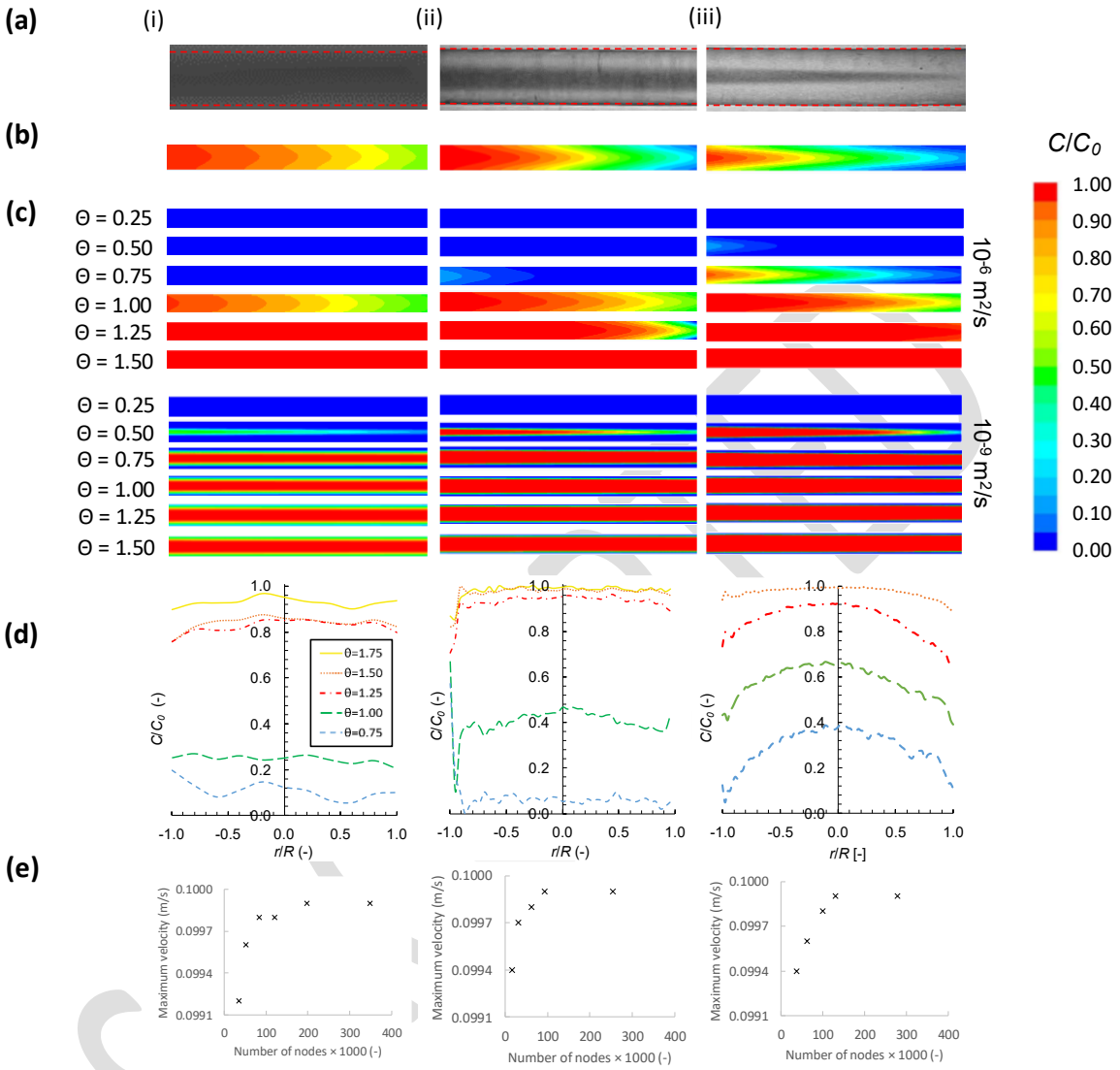

Figure 1

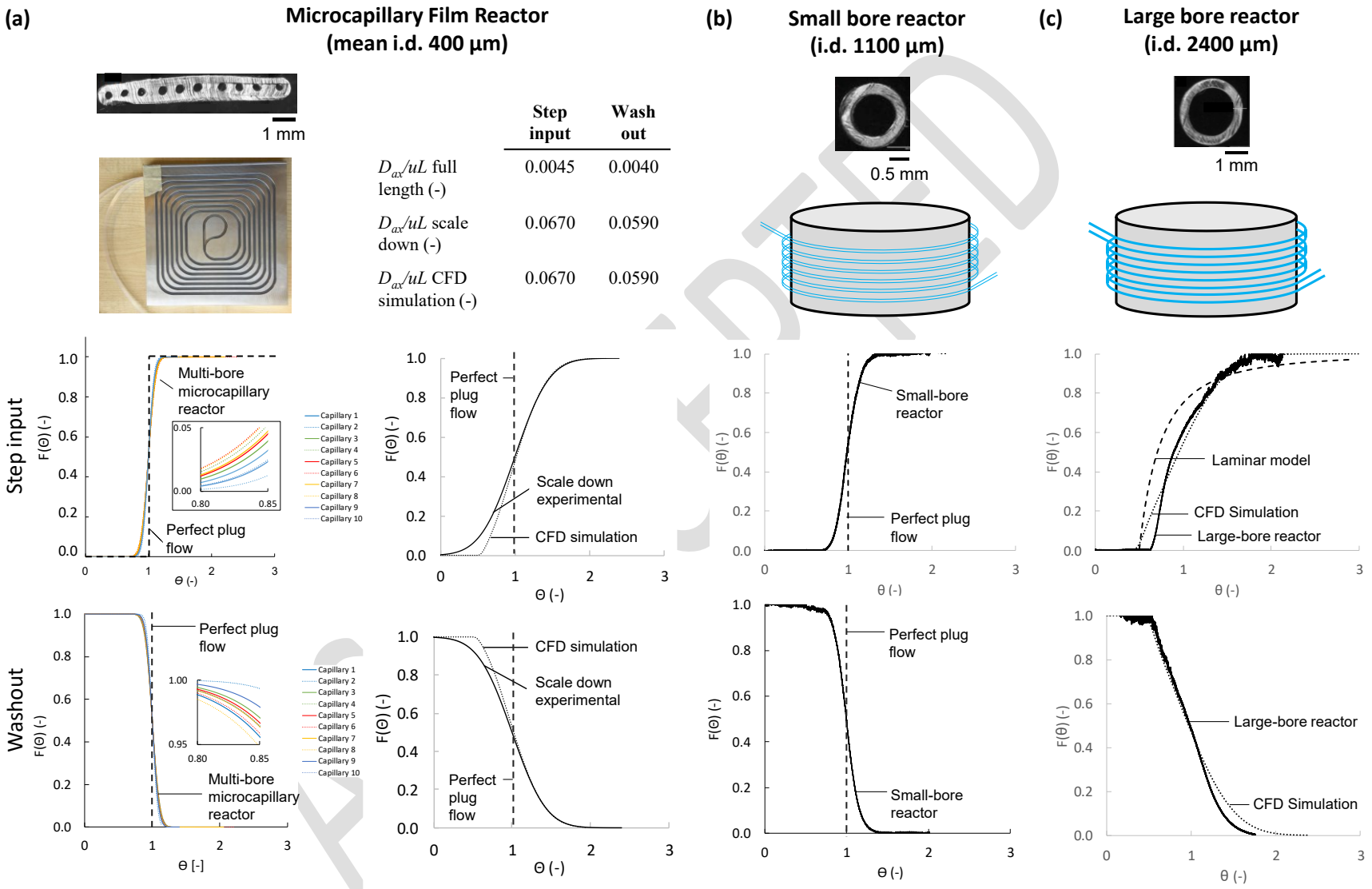

	Step input	Wash out
D_{ax}/uL full length (-)	0.0045	0.0040
D_{ax}/uL scale down (-)	0.0670	0.0590
D_{ax}/uL CFD simulation (-)	0.0670	0.0590

Figure 2

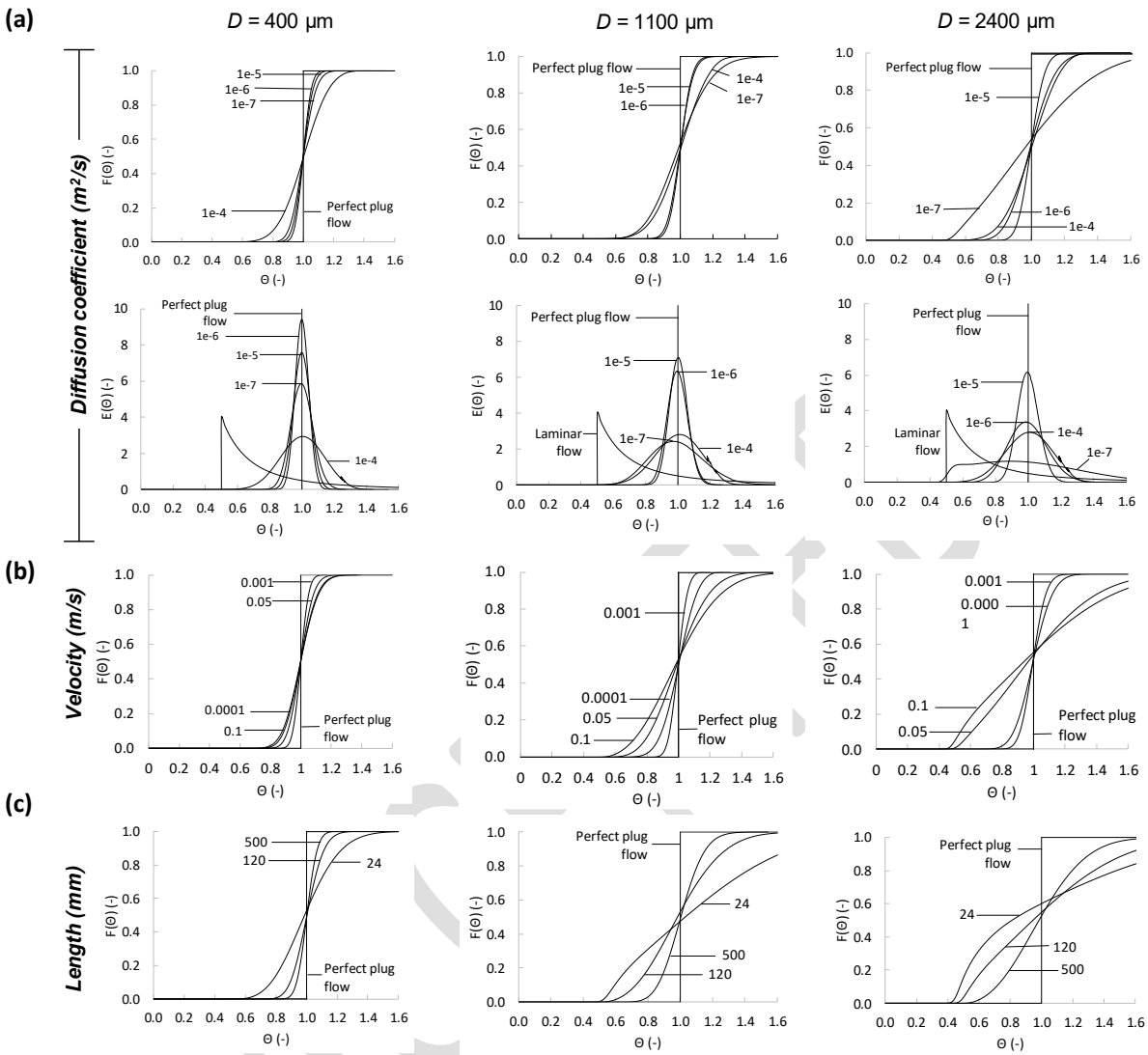
(a)
D = 400 µm
D = 1100 µm
D = 2400 µm
Diffusion coefficient (m²/s)
F(Θ) (-)
E(Θ) (-)
Θ (-)
1e-5
1e-6
1e-7
1e-4
Perfect plug flow
Laminar flow
(b)
Velocity (m/s)
0.001
0.05
0.0001
0.1
0.000 1
(c)
Length (mm)
500
120
24

Figure 3

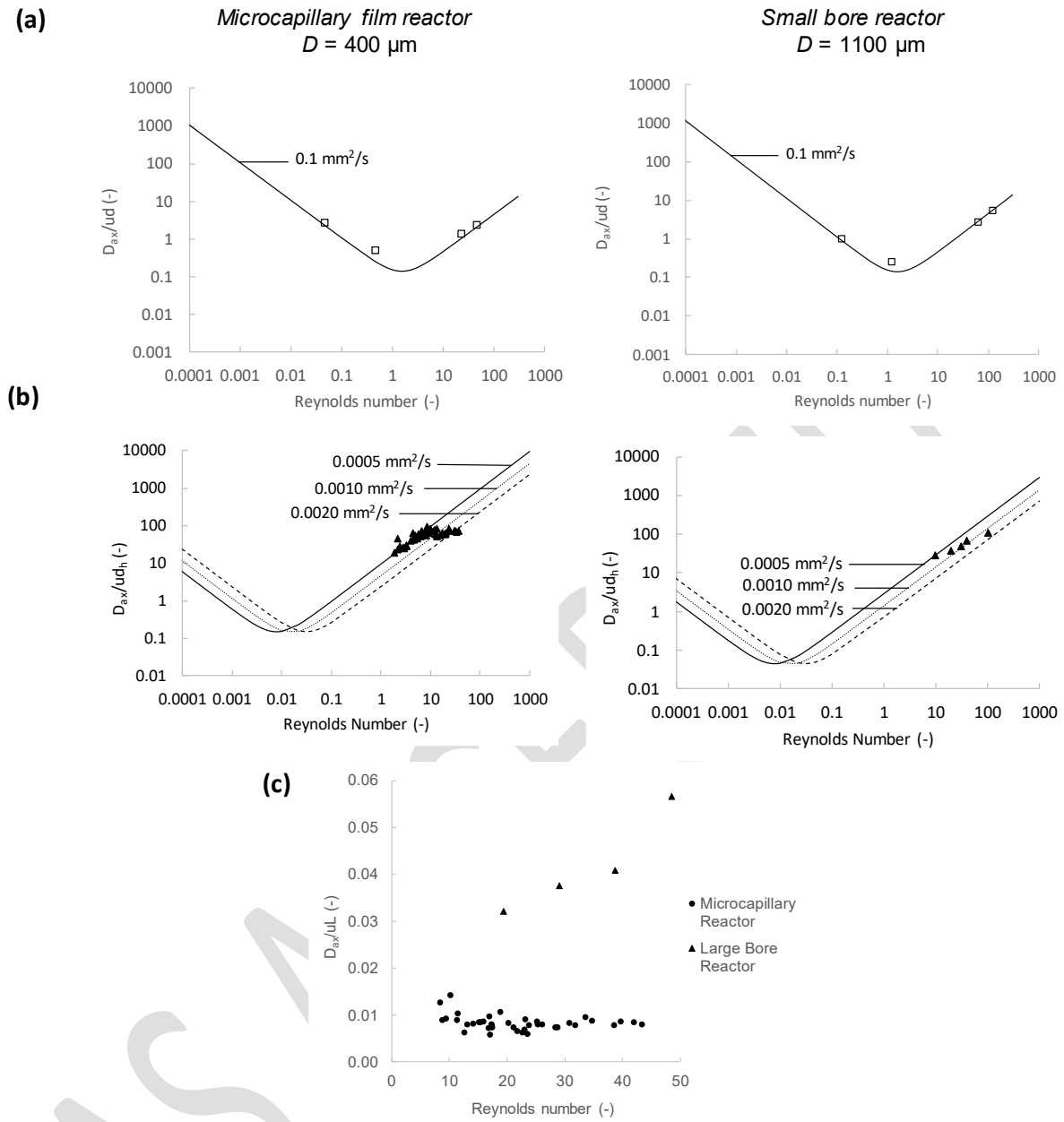
(a)
Microcapillary film reactor
D = 400 µm
Small bore reactor
D = 1100 µm
0.1 mm²/s
Dax/ud (-)
Reynolds number (-)
(b)
0.0005 mm²/s
0.0010 mm²/s
0.0020 mm²/s
Dax/udh (-)
Reynolds Number (-)
(c)
Dax/uL (-)
Microcapillary Reactor
Large Bore Reactor
Reynolds number (-)

Figure 4

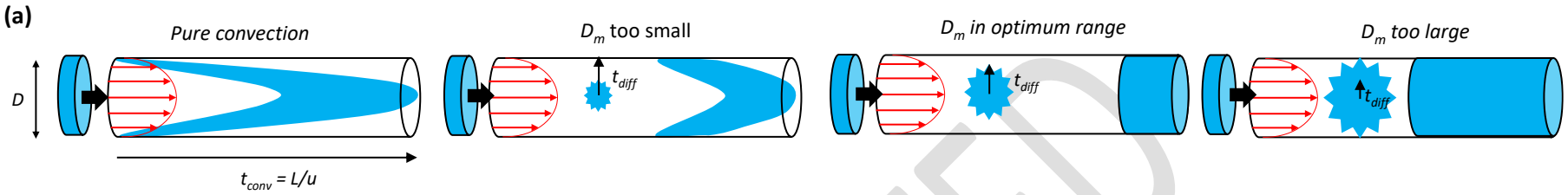

(b)

		Θ_B (-) D (µm)			= t_{conv} (s) D (µm)			+ t_{diff} (s) D (µm)			+ t_{diff} / t_{conv} (-) D (µm)		
		400	1100	2400	400	1100	2400	400	1100	2400	400	1100	2400
D_m (m²/s)	1.E-04	0.7	0.66	0.64	4.8	4.8	4.8	2.0E-04	1.5E-03	7.2E-03	4.2E-05	3.2E-04	1.5E-03
	1.E-05	0.87	0.86	0.82	4.8	4.8	4.8	2.0E-03	1.5E-02	7.2E-02	4.2E-04	3.2E-03	1.5E-02
	1.E-06	0.9	0.86	0.72	4.8	4.8	4.8	2.0E-02	1.5E-01	7.2E-01	4.2E-03	3.2E-02	1.5E-01
	1.E-07	0.86	0.66	0.5	4.8	4.8	4.8	2.0E-01	1.5E+00	7.2E+00	4.2E-02	3.2E-01	1.5E+00
u (m/s)	0.1000	0.8	0.57	0.47	2.4	2.4	2.4	2.0E-01	1.5E+00	7.2E+00	8.3E-02	6.3E-01	3.0E+00
	0.0500	0.83	0.67	0.49	4.8	4.8	4.8	2.0E-01	1.5E+00	7.2E+00	4.2E-02	3.2E-01	1.5E+00
	0.0010	0.9	0.88	0.86	240	240	240	2.0E-01	1.5E+00	7.2E+00	8.3E-04	6.3E-03	3.0E-02
	0.0001	0.8	0.78	0.78	2400	2400	2400	2.0E-01	1.5E+00	7.2E+00	8.3E-05	6.3E-04	3.0E-03
L (mm)	500	0.88	0.75	0.58	10	10	10	2.0E-01	1.5E+00	7.2E+00	2.0E-02	1.5E-01	7.2E-01
	120	0.81	0.58	0.55	4.8	4.8	4.8	2.0E-01	1.5E+00	7.2E+00	8.3E-02	6.3E-01	3.0E+00
	24	0.63	0.5	0.5	0.48	0.48	0.48	2.0E-01	1.5E+00	7.2E+00	4.2E-01	3.2E+00	1.5E+01

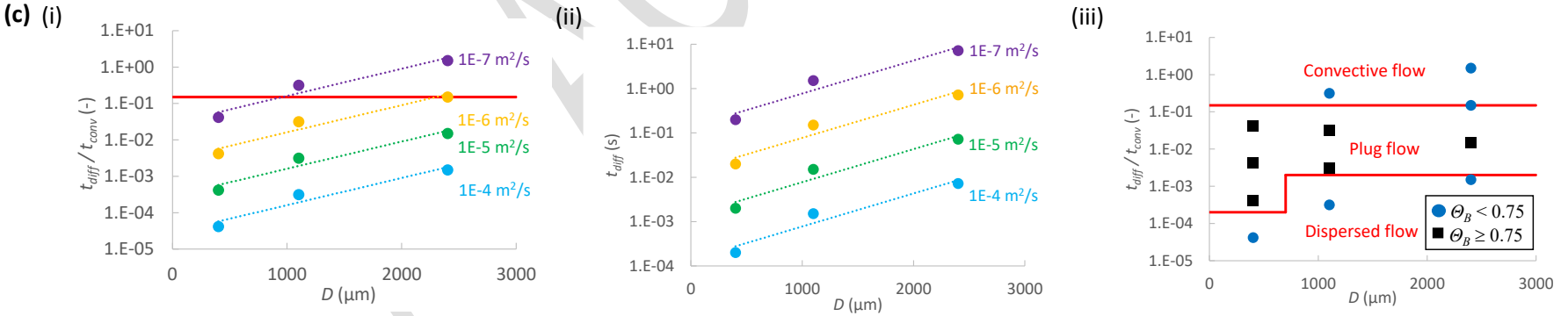

Figure 5

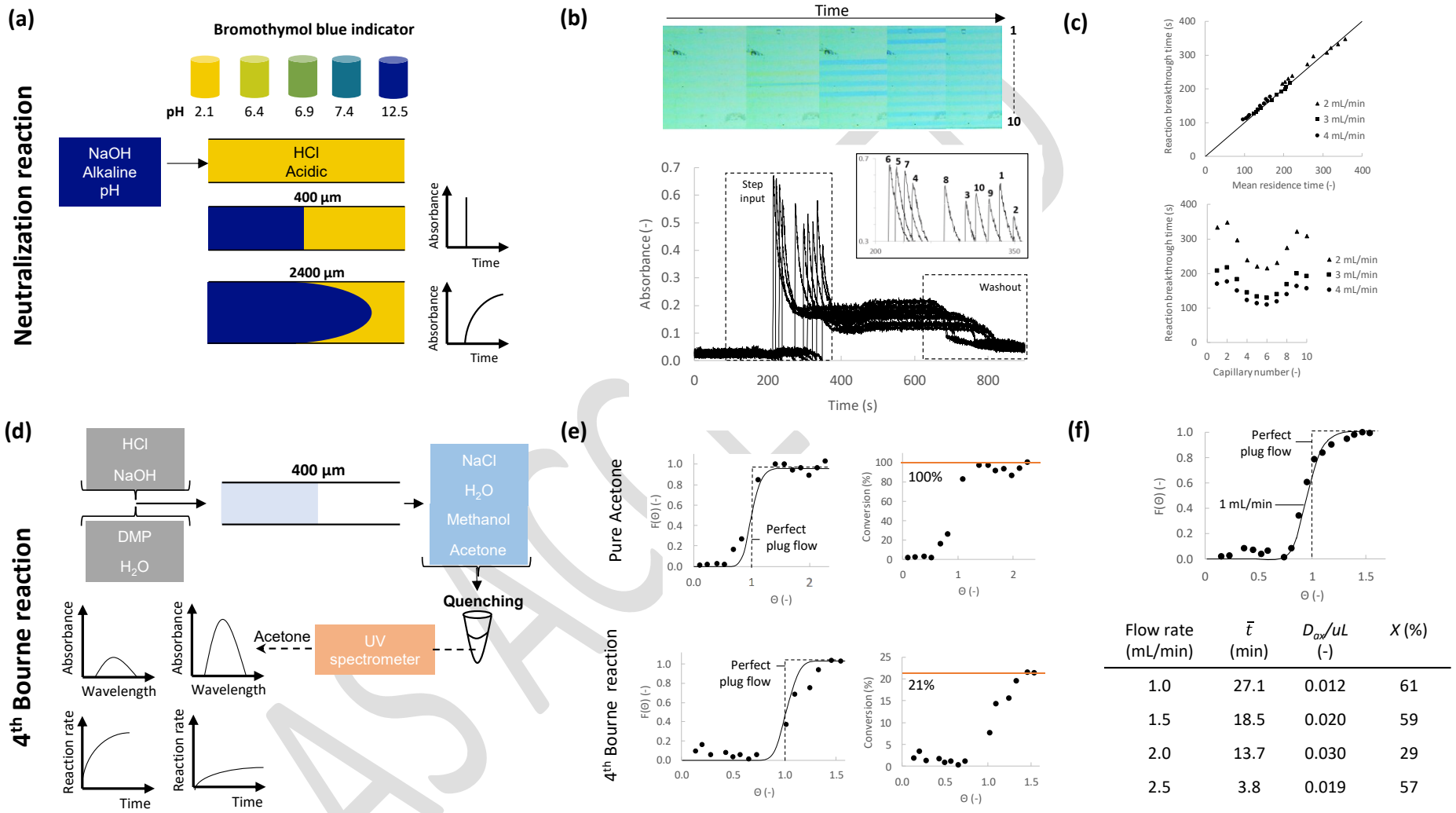

Flow rate (mL/min)	$\bar{t}$ (min)	D_{ax}/uL (-)	X (%)
1.0	27.1	0.012	61
1.5	18.5	0.020	59
2.0	13.7	0.030	29
2.5	3.8	0.019	57

Figure 6